Optics Letters

Dual-frequency Doppler lidar for wind detection with a superconducting nanowire single-photon detector

Mingjia Shangguan,[1,2,3] Haiyun Xia,[1,3,5] Chong Wang,[1] Jiawei Qiu,[1] Shengfu Lin,[1] Xiankang Dou,[1,4,6] Qiang Zhang,[2,3] and Jian-Wei Pan[2,3]

[1]CAS Key Laboratory of Geospace Environment, University of Science and Technology of China, Hefei 230026, China
[2]Shanghai Branch, National Laboratory for Physical Sciences at Microscale and Department of Modern Physics, USTC, Shanghai 201315, China
[3]Synergetic Innovation Center of Quantum Information and Quantum Physics, USTC, Hefei 230026, China
[4]Wuhan University, Wuhan 430072, China
[5]e-mail: hsia@ustc.edu.cn
[6]e-mail: dou@ustc.edu.cn

Received 18 May 2017; revised 4 August 2017; accepted 6 August 2017; posted 7 August 2017 (Doc. ID 296302); published 6 September 2017

A dual-frequency direct detection Doppler lidar is demonstrated using a superconducting nanowire single-photon detector (SNSPD) at 1.5 μm. The so-called double-edge technique is implemented by using a dual-frequency laser pulse, rather than using a double-channel Fabry–Perot interferometer. Such a modification to the reported lidars enhances the frequency stability in the system level. Using the time-division multiplexing method, only one piece of SNSPD is used in the optical receiver, making the system simplified and robust. The SNSPD is adopted to enhance the temporal resolution since it offers merits of high quantum efficiency, low dark count noise, no after-pulsing probability, and a high maximum count rate. Two telescopes that point westward and northward at a zenith angle of 30° are used to detect the line-of-sight wind components, which are used to synthesize the horizontal wind profile. Horizontal wind profiles up to an altitude of about 2.7 km are calculated with vertical spatial/temporal resolution of 10 m/10 s. Wind dynamic evolution and vertical wind shears are observed clearly.

OCIS codes: (010.3640) Lidar; (010.0280) Remote sensing and sensors; (030.5260) Photon counting; (280.3340) Laser Doppler velocimetry.

https://doi.org/10.1364/OL.42.003541

The detection of atmospheric hazards such as wind shear, wake vortex, and clear air turbulence is of importance for flight safety and increasing airport capacity [1]. Doppler wind lidar is an effective instrument to make range-resolved wind detection via Mie or Rayleigh backscattering in clear-air conditions [2,3]. For the past few decades, coherent detection lidars (CDLs) using either continuous wave or pulsed lasers, have been demonstrated for the detection of wind shears [4,5], aircraft wake vortices [6,7], turbulences [8,9], microbursts and wind gusts [10], and gravity waves [11].

In order to detect small-scale and fast wind evolution, both high spatial and high temporal resolutions are of key importance. For example, for estimating the aircraft wake vortex parameters, the spatial resolution should be less than the wingspan of the aircraft [12], on the order of a few to tens of meters. To improve the spatial resolution of a CDL, a laser pulse with narrower duration is generally used, at the sacrifice of the heterodyne efficiency, due to the spectrum broadening of the short laser pulse [13]. One should note that the direct detection lidar (DDL) can retrieve the Doppler shift carried on an atmospheric backscattering with a very broad spectrum. For example, even the bandwidth of the Rayleigh backscattering approaches a few gigahertz at 355 nm (full width at half-maximum [FWHM] = 3.8 GHz at 290 K), and a wind field in the mid-altitude can be detected [3,14,15]. In fact, a DDL can achieve high spatial resolution wind detection by optimizing the response function of a frequency discriminator for a short laser pulse.

In the DDL, the so-called double-edge technique is widely used to detect the Doppler shift. A multi-channel Fabry–Perot interferometer (FPI) is commonly used to realize the double-edge technique [2,3,14,15]. However, the common usage of a free-space FPI leads to great challenges, including complications in manufacturing, difficulty in precise alignment and parallelism controlling, and instability in harsh environments. To solve this problem, a convert single-channel all-fiber FPI has been demonstrated recently [16]. The transmitted and reflected backscattering signals from the FPI are detected. However, the background noises, including solar background noise and amplified spontaneous emission (ASE) noise of the laser are not suppressed in the reflection channel of the FPI. As a coaxial telescope is used, the ASE noise will be reflected from the mirrors into the detector, so that the laser should be purified [16]. Note that, in order to realize the double-edge technique with

only one transmission function of a single-channel FPI, a scheme that uses a dual-frequency laser has been proposed and simulated at 852 nm [17]. Since the transmission channel of the FPI can provide bandwidths as narrow as about 100 MHz, the background noise can be further filtered after passing through the FPI [18]. In this Letter, the dual-frequency scheme is adopted to realize wind detection with a superconducting nanowire single-photon detector (SNSPD) at 1.5 μm. As the detector is considered, an InGaAs avalanche photodiode is widely used for 1.5 μm detection. However, it suffers from low efficiency (10%), high noise (950 cps), low maximum count rate (1.6 Mcps), and high after-pulsing possibility (18%), and a specific algorithm should be performed for after-pulse and count rate corrections in lidar applications [19]. Thanks to the high quantum efficiency (60%) and low dark count rate (300 cps) of the SNSPD [20], the weak backscattering can be detected with a high signal-to-noise ratio. Another attractive feature of the SNSPD is its high maximum count rate, which is of importance for lidar applications because the atmospheric backscattering decays rapidly along a detection range, making the backscattering have a large dynamic range. Therefore, a high maximum count rate can avoid detector saturation, particularly in the near range.

Figure 1 presents two different schemes to realize the double-edge technique. As shown in Fig. 1(a), the commonly used scheme adopts a twin-channel FPI, serving as a frequency discriminator. The frequency of the outgoing laser is locked at the cross-point of the two transmission curves. By measuring the transmission changes of the Mie backscattering signals through the two channels of the FPI, a Doppler shift can be retrieved. In this Letter, the double-edge technique is realized with a dual-frequency laser that alternates the outgoing laser pulse on either the rising or the falling edges of a single-channel FPI, as shown in Fig. 1(b). Note that, in the twin-channel scheme (or two FPI scheme), the frequency separation of the two transmission curves is affected by many factors, such as the angle of the incident light, the parallelism error of the plates, and the temperature gradient and pressure fluctuation inside the FPI [2]. In contrast, in this dual-frequency scheme, the frequency offset of the laser pulses is determined by the radio-frequency (RF) frequency fed to an acousto-optic modulator (AOM), where a frequency accuracy of kilohertz is realized.

A schematic diagram of the Doppler lidar using a SNSPD (single quantum, Eos 210C) is shown in Fig. 2. The continuous-wave (CW) laser at the wavelength of 1548.1 nm is alternatively switched between a tunable attenuator (TA_1) and a fiber-coupled AOM by an optical switch (OS_1), entering an electro-optic modulator (EOM) as a CW beam switching between the unshifted (f_0) and upshifted ($f_s = f_0 + 80$ MHz) frequencies every 54 μs. The EOM then chops the CW laser with alternate frequencies into pairs of laser pulses. The time between individual pulses is set to be 27 μs, which corresponds to the maximum unambiguous detection range of 4.05 km. The laser pulse is amplified by a pre-amplifier (pre-erbium-doped fiber amplifier [EDFA]). The ASE emission from the pre-EDFA is filtered out by inserting a fiber Bragg grating (FBG) with a bandwidth of 8 pm.

As shown in Fig. 3, the period of the EOM is set to a quarter of the period of the AOM, which has the same period as the OS_1. In this Letter, one cycle of wind detection consists of four pulses. The odd pulses picked out by the OS_2 are amplified by the $EDFA_1$ and sent to the atmosphere through the westward telescope, while the even pulses selected by OS_2 are amplified by another $EDFA_2$ before sending to northward telescope. The two telescopes that point to different directions at the zenith angle of 30° are used to detect the orthogonal components of the horizontal wind. The pulse energy is set to 50 μJ. The FWHM of the laser pulse is set to 77 ns. Taking the zenith angle into account, the vertical spatial resolution is 10 m. Since the OS_2 is used to alternate the outgoing laser pulse between the two telescopes, only one SNSPD can realize the atmospheric wind detection. Compared with the lidar system that

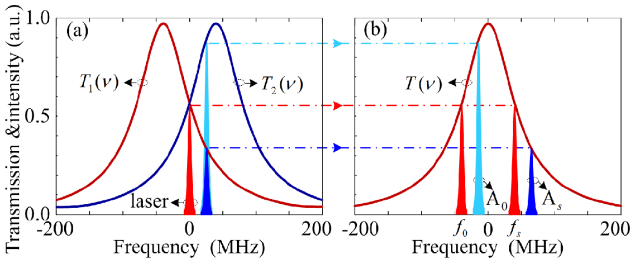

Fig. 1. Double-edge technique that adopts (a) a double-channel FPI and (b) a dual-frequency laser pulse.

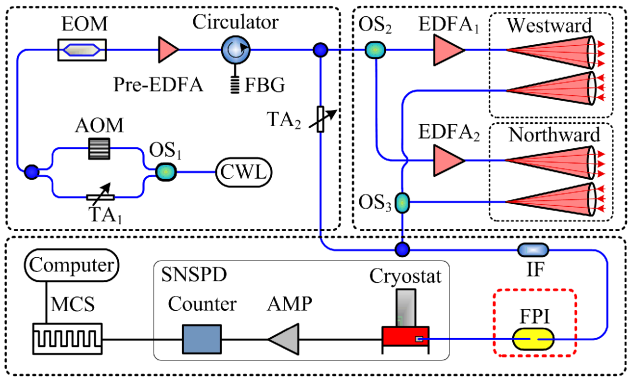

Fig. 2. Schematic setup of the Doppler lidar. OS, optical switch; AOM, acousto-optic modulator; TA, tunable attenuator; EOM, electro-optic modulator; EDFA, erbium-doped fiber amplifier; FBG, fiber Bragg grating; OS, optical switcher; IF, interference filter; FPI, Fabry–Perot interferometer; SNSPD, superconducting nanowire single-photon detector; AMP, amplifier; MCS, multi-channel scaler.

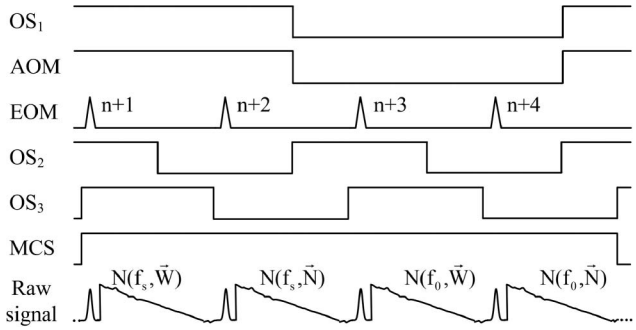

Fig. 3. Timing sequence of the data acquisition of one wind detection cycle.

uses a set of telescope and scanner [16], such an optical layout saves time in mechanical scanning process.

As shown in Fig. 3, the atmospheric backscattering signals collected by the telescopes (80 mm diameter), labeled as $N(f_s, \vec{W})$, $N(f_s, \vec{N})$, $N(f_0, \vec{W})$, and $N(f_0, \vec{N})$, are selected by OS_3 and fed to the optical receiver in sequence. Here, the OS_3 is used instead of using a 3 dB fiber coupler, since the optical switch provides a −35 dB suppression of the background noise from the other telescope. It only introduces an insertion loss of 0.8 dB.

A small fraction of the laser energy is split out and attenuated to a single-photon level as a reference laser. The background noise is filtered out by inserting an interference filter (IF) with a bandwidth of 0.3 nm. An all-fiber lensless FPI with a free spectral range of 4.02 GHz is used as a frequency discriminator. A line-of-sight wind velocity of 1 m/s will cause a Doppler shift in frequency domain of 1.29 MHz at 1548 nm. The FWHM of the FPI is 97.6 MHz, which is optimized to cover a dynamic range of about ±35 m/s for wind measurement in the atmospheric boundary layer [21]. The frequency scanning of the FPI can be achieved by scanning its cavity length at a fixed laser frequency [2,22]. A stacked piezoelectric transducer (PZT) that axially strains a single-mode fiber inserted in the cavity will change the cavity length. The transmitted backscattering signals through the FPI are coupled into the SNSPD, which has a detection efficiency of 60% and a dark count rate of 300 cps. The TTL signals corresponding to the photons received on the SNSPD are recorded on a multichannel scaler (MCS) and then processed in a computer.

In this Letter, the response function is defined as

$$Q(\nu) = [T_0(\nu) - T_s(\nu)]/[T_0(\nu) + T_s(\nu)], \quad (1)$$

where $T_0(\nu)$ and $T_s(\nu)$ are the transmission functions of backscattering through the FPI when the non-frequency-shifted (f_0) and upshifted (f_s) lasers are used, respectively.

By scanning the voltage fed to the PZT in the FPI, the transmission curves are measured by using the dual-frequency pulsed lasers over 10 days, as shown in Fig. 4(a). The frequency in Fig. 4 is defined relative to the middle frequency of the dual-frequency laser. The frequency separation of the two transmission curves is equal to the frequency offset of the dual-frequency laser. The frequency offset of 80 MHz is determined by the RF frequency fed to the AOM. This value is adopted as a scale reference to perform the voltage to frequency conversion in the calibration. The measured transmission values are normalized and then fitted to Voigt functions. Two typical fitted curves are plotted in Fig. 4(a). The fitting residuals are less than ±2%, as shown in Fig. 4(b). The mean FWHM of the fitting transmission curves is 98 MHz, with a relative error less than 0.1%. Taking into account this measurement precision in the calibration process, a systematic wind error less than 0.06 m/s is introduced in the frequency range of −45 to 45 MHz. [23]. To measure the wind speed, the frequency of the output laser is locked at the cross-point, where the sensitivity is maximized. A small fraction of the laser energy is split out as the reference signal, realizing a frequency locking of the laser to the FPI with a precision of 0.1 MHz (equals 0.08 m/s) over every second. Finally, the response values are calculated using Eq. (1) and plotted in Fig. 4(c).

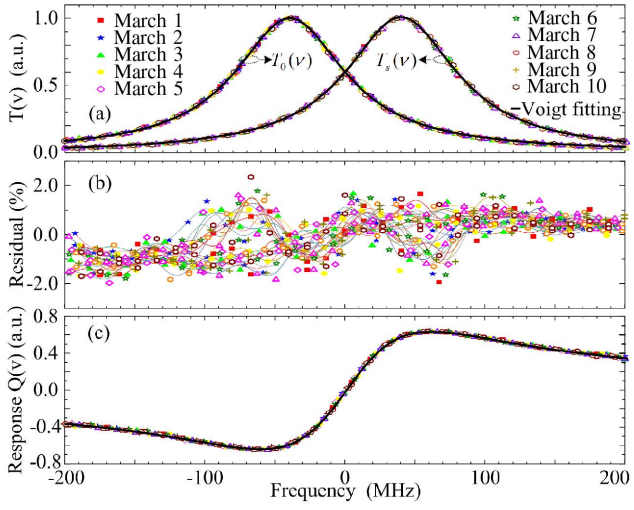

Fig. 4. (a) Transmission curves measured in March 2017 and typical Voigt fitting curves (solid line), (b) residuals that are relative to the peaks, and (c) calculated response functions that were measured over 10 days. The symbols represent the measured data, and the black lines represent their fitting results.

A field experiment was carried out at the campus of our university (31.843°N, 117.265°E). The experiment started at 17:00 and ended at 18:00 on March 15, 2017. The experimental raw data with 10 s temporal resolution are plotted in Fig. 5. The intensity of the backscattering signals varies significantly over 1 h because the experiment was performed just before a thunder shower occurred at 18:00. The raw signals dropped suddenly at the altitude of about 1.5 km from 17:12 to 17:36 due to the sharp decrease in aerosol concentration. A nimbus cloud is detected at the altitude of about 2.6 km.

Figure 6 shows a typical detection result. The error bars are calculated with an assumption that the detection noise is dominated by the photon-counting fluctuation following a Poisson distribution [2]. The tolerated error of the radial wind is 2 m/s in this Letter. The wind direction is defined as a clockwise angle with respect to the north direction. To validate the accuracy of the measurement, the horizontal wind results from the lidar are compared with the results from an ultrasonic wind sensor (Vaisala windcap WMT52), as we did in the previous work [16].

The wind evolution in the atmospheric boundary layer before a thunder shower is captured. The horizontal wind speed and direction are calculated from the meridional wind and zonal wind, as shown in Fig. 7. Note that, when retrieving the horizontal wind, the vertical wind should be taken into account. In this Letter, the wind is assumed to be horizontally

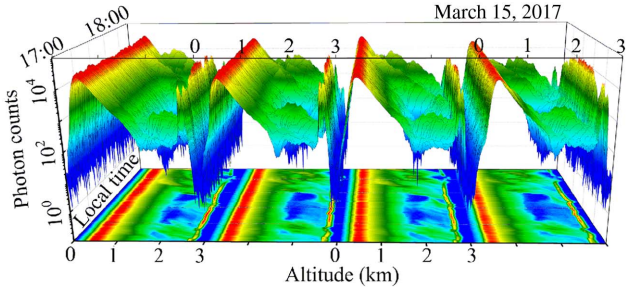

Fig. 5. Raw lidar signals over 1 h, from left to right: $N(f_s, \vec{W})$, $N(f_s, \vec{N})$, $N(f_0, \vec{W})$ and $N(f_0, \vec{N})$.

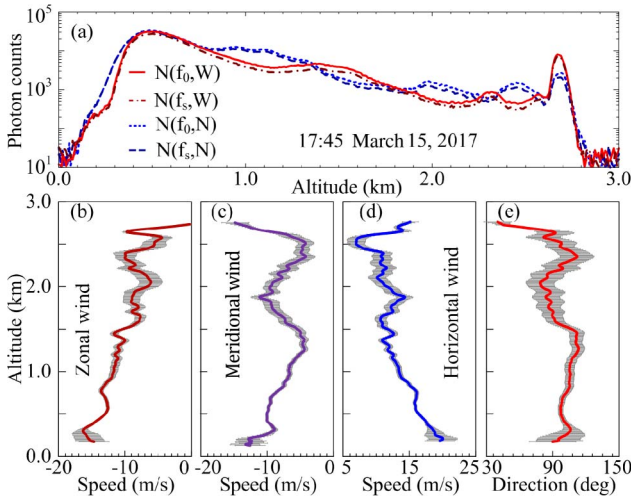

Fig. 6. (a) Raw lidar signals, (b) zonal wind, (c) meridional wind, (d) horizontal wind, and (e) wind direction at 17:45, on March 15, 2017.

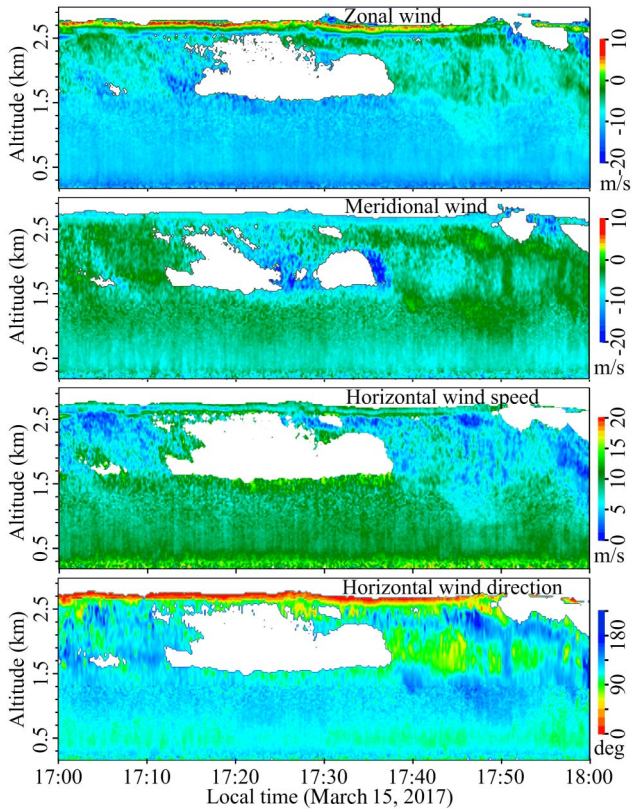

Fig. 7. One-hour observation results, from top to bottom: zonal wind, meridional wind, horizontal wind speed, and wind direction.

homogeneous with a negligible vertical component. A nimbus at an altitude of 2.6 km comes from the north. The wind turns to the east beneath the nimbus. The layered dynamic structure of the nimbus is observed, with a speed higher than that just beneath the rain clouds.

In conclusion, a dual-frequency direct detection Doppler wind lidar, incorporating a SNSPD is demonstrated for wind detection up to an altitude of 2.7 km, with a 10 m vertical spatial and 10 s temporal resolution. A single-channel FPI and a dual-frequency laser are adopted to realize the double-edge technique, incorporating a time-division multiplexing method. This scheme has excellent performance in suppressing the background noise and the ASE noise of the laser. Furthermore, such an implementation simplifies the system greatly and enhances its stability. In the field experiment, wind shear in speed and direction versus altitude are detected.

REFERENCES

1. C. Besson, A. Dolfi-Bouteyre, G. Canat, N. Cézard, B. Augère, A. Durecu, L. Lombarb, M. Valla, and A. Hallermeyer, Aerosp. Lab **12**, 1 (2016).
2. H. Xia, D. Sun, Y. Yang, F. Shen, J. Dong, and T. Kobayashi, Appl. Opt. **46**, 7120 (2007).
3. H. Xia, X. Dou, D. Sun, Z. Shu, X. Xue, Y. Han, and T. Cheng, Opt. Express **20**, 15286 (2012).
4. C. M. Shun and P. W. Chan, J. Atmos. Ocean. Technol. **25**, 637 (2008).
5. S. C. Tucker, W. A. Brewer, R. M. Banta, C. J. Senff, S. P. Sandberg, D. C. Law, A. M. Weickmann, and R. M. Hardesty, J. Atmos. Ocean. Technol. **26**, 673 (2009).
6. F. Köpp, S. Rahm, and I. Smalikho, J. Atmos. Ocean. Technol. **21**, 194 (2004).
7. A. Dolfi-Bouteyre, G. Canat, M. Valla, B. Augere, C. Besson, D. Goular, L. Lombard, J. Cariou, A. Durecu, D. Fleury, L. Bricteux, S. Brousmiche, S. Lugan, and B. Macq, IEEE J. Sel. Top. Quantum Electron. **15**, 441 (2009).
8. I. N. Smalikho, F. Köpp, and S. Rahm, J. Atmos. Ocean. Technol. **22**, 1733 (2005).
9. V. A. Banakh, I. N. Smalikho, and S. Rahm, Opt. Lett. **39**, 4321 (2014).
10. G. J. Koch, J. Y. Beyon, B. W. Barnes, M. Petros, J. Yu, F. Amzajerdian, M. J. Kavaya, and U. N. Singh, Opt. Eng. **46**, 016002 (2007).
11. B. Witschas, S. Rahm, A. Dörnbrack, J. Wagner, and M. Rapp, J. Atmos. Ocean. Technol. **34**, 1371 (2017).
12. I. N. Smalikho and V. A. Banakh, Opt. Lett. **40**, 3408 (2015).
13. B. J. Rye and R. M. Hardesty, IEEE Trans. Geosci. Remote Sens. **31**, 16 (1993).
14. H. Xia, X. Dou, M. Shangguan, R. Zhao, D. Sun, C. Wang, J. Qiu, Z. Shu, X. Xue, Y. Han, and Y. Han, Opt. Express **22**, 21775 (2014).
15. O. Reitebuch, C. Lemmerz, E. Nagel, U. Paffrath, Y. Durand, M. Endemann, F. Fabre, and M. Chaloupy, J. Atmos. Ocean. Technol. **26**, 2501 (2009).
16. H. Xia, M. Shangguan, C. Wang, G. Shentu, J. Qiu, J. Zhang, Q. Zhang, X. Dou, and J. Pan, Opt. Lett. **41**, 5218 (2016).
17. J. T. Dobler, B. M. Gentry, and J. A. Reagan, Proc. SPIE **4484**, 82 (2002).
18. U. von Zahn, G. von Cossart, J. Fiedler, K. H. Fricke, G. Nelke, G. Baumgarten, D. Rees, A. Hauchecorne, and K. Adolfsen, Ann. Geophys. **18**, 815 (2000).
19. C. Yu, M. Shangguan, H. Xia, J. Zhang, X. Dou, and J. Pan, Opt. Express **25**, 14611 (2017).
20. C. M. Natarajan, M. G. Tanner, and R. H. Hadfield, Supercond. Sci. Technol. **25**, 063001 (2012).
21. C. L. Korb, B. M. Gentry, S. X. Li, and C. Flesia, Appl. Opt. **37**, 3097 (1998).
22. M. Shangguan, H. Xia, C. Wang, J. Qiu, G. Shentu, Q. Zhang, X. Dou, and J. Pan, Opt. Express **24**, 19322 (2016).
23. M. Shangguan, H. Xia, X. Dou, C. Wang, J. Qiu, Y. Zhang, Z. Shu, and X. Xue, Chin. Phys. B **24**, 094212 (2015).